

ATMOSPHERIC GAMMA-RAY AND NEUTRON FLASHES

*L. P. Babich**, *A. Yu. Kudryavtsev***, *M. L. Kudryavtseva***, *I. M. Kutsyk*

*Russian Federal Nuclear Center
All-Russian Research Institute of Experimental Physics (VNIIEF)
607188, Sarov, Russia*

Received May 3, 2007

Gamma-ray pulses are calculated from 2D numerical simulations of the upward atmospheric discharge in a self-consistent electric field using the multi-group approach to the kinetics of relativistic runaway electrons (REs). Computed γ -ray numbers and spectra are consistent with those of terrestrial γ -ray flashes (TGFs) observed aboard spacecrafts. The RE flux is concentrated mainly within the domain of the Blue Jet fluorescence. This confirms that exactly the domain adjacent to a thundercloud is the source of the observed γ -ray flashes. The yield of photonuclear neutrons is calculated. One γ -ray pulse generates $\sim 10^{14}$ – 10^{15} neutrons. The possibility of direct deposition of REs to the detector readings and the origin of the lightning-advanced TGFs are discussed.

PACS: 92.60.Pw, 52.80.Mg

1. INTRODUCTION

Since the 1930s, experiments were being conducted to detect high-energy electromagnetic phenomena related to thunderstorm activity in the atmosphere. These phenomena ensue from the electron acceleration to high energies in a thunderstorm atmosphere predicted by Wilson [1] and termed the “electron runaway” by Eddington [2]. Results obtained until the end of the 1980s are reviewed in book [3]. During recent decades, the occurrence of such phenomena was firmly established. Up to three orders of the value increase of the penetrating radiation (X-rays) inside thunderclouds was detected by airborne instruments above the fine-weather background [3–6]. Terrestrial γ -ray flashes (TGFs) observed aboard artificial satellites BETSI [7] and RHESSI [8] are another high-energy phenomenon. The most frequently discussed mechanism of TGFs assumes γ -ray production by gigantic upward atmospheric discharges (UADs) originating from the electrical breakdown driven by relativistic runaway electrons (REs) [9–12].

A statistically significant amplification of the atmospheric neutron flux over the cosmic-ray background detected in the lower troposphere during thunderstorm activity [13–15] is yet another high-energy phe-

nomenon: terrestrial neutron flashes (TNFs). Following [16, 17], the TNFs were interpreted as a result of nuclear synthesis ${}^2\text{H}({}^2\text{H}, n){}^3\text{He}$ in a lightning channel. But nuclear fusion is absolutely impossible under physical conditions that exist in the channel according to the contemporary knowledge, and the neutrons could be generated by photonuclear reactions (γ, n) accompanying TGFs [18–20]. In the framework of the UAD analytic model with the geomagnetic field taken into account [21, 22], the (γ, n) yield was estimated as $\sim 10^{15}$ neutrons per UAD [18–20].

Proceeding from Wilson’s idea that at high altitudes the reduced strength of the thundercloud electric field E/P can be above the threshold required for the conventional quasistatic breakdown [23], a mechanism of discharges in the upper stratosphere/lower ionosphere is being developed, including the conventional breakdown by electrons with energies in the vicinity of the ionization threshold in a strong electric field triggered high above the thundercloud by lightning discharges in the troposphere (see, e.g., [24–31]). In the framework of this approach, the high-altitude optical phenomena above thunderstorms (Blue Jets, Red Sprites, etc. [32–35]) can be described more or less adequately, but difficulties appear with TGFs and TNFs. Electron energizing up to 2–8 keV predicted in the enhanced field ahead of the streamer front [30] is too small to account even for the X-rays [3–6], to say nothing of TGFs [7,

*E-mail: babich@elph.vniief.ru

**E-mail: kay@sar.ru

8] and TNFs [13–15]. To bypass this difficulty, Moss et al. [30] performed calculations to justify the hypothesis of electron energizing up to tens MeV in a rather weak but extended field near the lightning leader [30]. More rigorous analysis and numerical simulations are required to prove or reject this attractive hypothesis. A very interesting model in which REs acquire large energies from the electromagnetic pulse generated by a horizontal lightning discharge and penetrating to the upper stratosphere [27, 28] requires taking the self-consistent field into account. Besides, the fractal approach implemented in the framework of the spherical approximation [28] needs more detailed substantiation because RE distributions in thunderstorm fields are strongly anisotropic [36].

Starting with the pioneering works [9, 10], an alternative mechanism of the breakdown in the atmosphere in a rather weak thundercloud field controlled by a series of relativistic RE avalanches (RREAs) is being developed. RREA generation enables the breakdown in fields with the strength significantly below the threshold required for the conventional breakdown. The capability to account for the high-altitude optical phenomena along with TGFs and TNFs in a unified manner is an advantage of the mechanism. Based on this mechanism, a theory of UAD is being developed (see review [11]) and numerical simulations are being conducted (see, e.g., [21, 22, 37–46]). The variety of simulated thundercloud charge configurations and durations of the lightning discharge triggering the breakdown leads to different RE space–time distributions. The variety is quite natural, because the observational data are not full enough for reliable selecting configurations that could account for both the high-altitude optical phenomena and the TGFs and TNFs, although the progress in this direction is doubtless [47, 48]. The results of TGF calculations in [21, 22, 37–39, 42–44, 49] agree with the BETSI data [7, 50], although out-of-date and strongly overestimated RREA rates were used except in [21, 22, 42, 43, 49]. The geomagnetic field was taken into account in [21, 22, 42], which is an obvious advantage, especially because the majority of TGFs were detected in the tropical zone [8]. Too large values of the adopted cloud charge $Q = 1200$ C and its size ~ 100 km is an obvious shortcoming of simulations in [42]. The charge was later reduced to $Q = 450$ C at the altitude $H = 15$ km [43].

In this paper, we concentrate on the mechanism assuming the UADs developing in the RREA mode to be the origin of TGF. As in our previous simulations [45, 46], we use a series of rather realistic values of Q and H . The process of switching on the electric field above

the cloud was also simulated. In contrast to recent papers [47, 49], the characteristics of BETSI [7] and RHESSI [8] TGFs were calculated based on the results of numerical simulations of UAD in a self-consistent electric field. In contrast to [18–20], the photonuclear neutron yields, presumably accounting for TNFs, were calculated using the computed hard bremsstrahlung (γ -ray source) responsible for the TGFs. Optical emissions were calculated with the goal to verify the model applicability by comparison with the observed Blue Jet and Red Sprite fluorescence [32].

2. NUMERICAL DISCHARGE MODEL

The model is a further development of the 1.5D model used earlier for simulating the high-altitude optical phenomena and distinguished for the multigroup fluid description of the RE kinetics [45, 46], although implemented in the framework of the RE current tube approximation with an a priori set discharge transverse size. Broadly used in the neutron transport simulations (see, e.g., [51]), the multigroup fluid techniques in general permit receiving a particle distribution not only in space and time but also by energies. Therefore, these techniques are similar to the direct kinetic equation approach, but are more efficient and time-saving for computer implementation. For the problem considered, the multigroup technique enables receiving RE energy distributions required for calculating the primary bremsstrahlung spectrum and accurately simulating the RE penetration to high altitudes. The latter is important for correctly calculating the γ -ray transport to space.

The multigroup technique is implemented in the framework of a consistently 2D fluid approach [52]. The RE population is distributed over energy groups in the range $[\varepsilon_{th}, \varepsilon_{max}]$, where ε_{max} is specified by the idiosyncrasy of the problem under consideration and ε_{th} is the runaway threshold, i.e., the second root of the equation $F(\varepsilon) = eE$ [53], where eE is the electric force and the drag force $F(\varepsilon)$ accounts for interactions of REs of energy ε with air molecules. The RE kinetics is described using a simplified set of rigorous group equations including the continuity equations, the energy balance equations, and the equations of motion [54]:

$$\begin{aligned} \frac{\partial n_{run}^{(n)}}{\partial t} + \nabla \cdot (n_{run}^{(n)} \mathbf{w}_{run}^{(n)}) = \\ = \delta_{n,1} R \sum_{i=n}^N n_{run}^{(i)} + S_{run} \delta_{n,1} - |A_{run}^{(n)}| + |A_{run}^{(neib)}|, \quad (1) \end{aligned}$$

$$\frac{\partial \varepsilon_{run}^{(n)}}{\partial t} = -e(\mathbf{E} \cdot \mathbf{w}_{run}^{(n)}) - F^{(n)} \frac{(w_{run}^{(n)})^2}{v_{run}^{(n)}}, \quad (2)$$

$$m \left(\frac{\partial \gamma^{(n)}(w_i)_{run}^{(n)}}{\partial t} + (\mathbf{w}_{run}^{(n)} \cdot \nabla \gamma^{(n)}(w_i)_{run}^{(n)}) \right) = -eE_i - (F)_{run}^{(n)} \frac{(w_i)_{run}^{(n)}}{v_{run}^{(n)}} n_{run}^{(n)}, \quad (3)$$

where $n \in [1, N]$ is the group number, $n_{run}^{(n)}$ is the concentration, $\mathbf{v}_{run}^{(n)}$ is the velocity, $\mathbf{w}_{run}^{(n)}$ is the directed velocity,

$$R(P, v_{run}, E) = v_{run} P [\text{atm}] / ct_{run}(\delta, P = 1 \text{ atm})$$

is the total rate of RE generation by REs themselves, P is the local pressure, $\delta = eE/F_{min}P$ is the ‘‘overvoltage’’ relative to the minimal value $F_{min} = 218 \text{ keV/m}\cdot\text{atm}$ of the drag force $F(\varepsilon)$, S_{run} is the external source of primary REs, δ_{n1} is the Kronecker symbol,

$$A_{run}^{(n)} = \frac{\partial \varepsilon_{run}^{(n)}}{\partial t} \frac{n_{run}^{(n)}}{\varepsilon_n - \varepsilon_{n-1}}$$

is the operator responsible for the RE outflow from a group n into groups $n-1$ or $n+1$,

$$A_{run}^{(neib)} = \begin{cases} A_{run}^{(n+1)}, A_{run}^{(n+1)} \leq 0, & 1 \leq n \leq N-1, \\ A_{run}^{(n-1)}, A_{run}^{(n-1)} \geq 0, & 2 \leq n \leq N \end{cases}$$

is the operator responsible for the RE inflow into the group n from the adjacent groups, m is the electron mass, and $\gamma^{(n)}$ is the Lorentz factor.

Equations (1) allow for that the secondary REs to be produced owing to the ionization by REs themselves and the external source to mainly populate the first group. In contrast to our earlier simulations [41, 45, 46], an accurate dependence of the RE multiplication time t_{run} on the ‘‘overvoltage’’ δ [36] was used.

Equations (3) are actually used only for simulating small sections of RE trajectories, where $eE > F(\varepsilon_{th})$ or $eE < F(\varepsilon_{th})$, along which electrons are respectively accelerated up to the velocity of light c or decelerated below the threshold ε_{th} to become low-energy secondary electrons. Thus, the inertia of the acceleration and stopping processes is taken into account within the framework of consistent hydrodynamics. This allows avoiding numerical instabilities arising if jump-like gaining the velocity c or braking to the drift domain is permitted. Preliminary calculations proved that the cumulative contribution of the convective terms in

Eqs. (3) is small in comparison with the force-term depositions. These terms were therefore omitted in finite-difference analogues of differential equations (3) to save the computation time.

Kinetics of secondary (s) and background (b) electrons of low energies and positive (+) nitrogen N_2^+ and negative (−) oxygen O_2^- ions was described by the drift approximation of the continuity equation allowing for the ionization by REs and low-energy electrons, recombination of electrons and ions, and the electron attachment to oxygen molecules, external sources (cosmic ray) of background electrons, and ions:

$$\frac{\partial n_s}{\partial t} + \nabla(n_s \mathbf{v}_s) = \nu_i n_s - b_{e+} n_s n_+ - \eta n_s + R_s n_{run} + A_{run}^{(1)}, \quad (4)$$

$$\frac{\partial n_b}{\partial t} + \nabla(n_b \mathbf{v}_b) = \nu_i n_b - b_{e+} n_b n_+ - \eta n_b + S_b, \quad (5)$$

$$\frac{\partial n_+}{\partial t} + \nabla(n_+ \mathbf{v}_+) = \nu_i (n_s + n_b) + S_{run} + S_b + S_- - b_{e+} (n_s + n_b) n_+ - b_{-+} n_- n_+ + (R + R_s) n_{run}, \quad (6)$$

$$\frac{\partial n_-}{\partial t} + \nabla(n_- \mathbf{v}_-) = \eta (n_s + n_b) - b_{-+} n_- n_+ + S_-. \quad (7)$$

Here, n_s , n_b , n_+ , and n_- are concentrations, \mathbf{v}_s , \mathbf{v}_b , $\mathbf{v}_+ = \mu_+ \mathbf{E}$, and $\mathbf{v}_- = -\mu_- \mathbf{E}$ are drift velocities, $\mu_{+,-}$ are the ion mobilities, ν_i is the frequency of molecule ionization by low-energy electrons, b_{e+} and b_{-+} are the recombination coefficients,

$$\eta = (K_{diss} + K_{thr} N(z)) N_{O_2}(z)$$

is the coefficient of electron attachment to oxygen molecules, K_{thr} and K_{diss} are the three-body and dissociative attachment coefficients, $N(z)$ and $N_{O_2}(z) = 0.2N(z)$ are concentrations of air and oxygen molecules, R_s is the rate of low-energy electron production by RE–molecule collisions, and S_b , S_- , and S_{run} are sources of background electrons, negative ions, and REs. Available literature data were used for v_s , v_b , $\mu_{+,-}$, ν_i , b_{e+} , b_{-+} , K_{thr} , and K_{diss} (see the references in [52]). For S_{run} , a formula was obtained [52] based on the published data on the cosmic ray flux [55]. Sources of background electrons S_b and negative ions S_- were obtained from the formulas for the atmosphere conductivity $\sigma(z)$ [10] and the concentration of background electrons [55]. The rate of low-energy electron generation by RE ionizing impacts was expressed as

$$R_s(z) = F_{min} P(z) c / \Delta \varepsilon_{ion} = 2.18 \cdot 10^{12} P [\text{atm}]$$

via the electron–ion pair “cost” $\varepsilon_{ion} \approx 32$ eV.

We note that the motion of ions was discounted both in our previous models [41, 45, 46] and in simulations of other authors. Allowing for this motion described by the second terms in Eqs. (6) and (7) is especially important for avoiding numerical instabilities in the vicinity of the disks (see below) modeling the cloud charges.

The initial conditions were as follows:

$$n_{run}^{(n)}(t=0) = 0, \quad n_s(t=0) = 0, \\ n_b(t=0) = 10^{4+(z[\text{km}]-60)/6.7}$$

for the night atmosphere and

$$n_b(t=0) = 10^{6+(z[\text{km}]-60)/10}$$

for the day atmosphere (an approximation of the data available in [56]),

$$n_+(t=0) = n_-(t=0) + n_b(t=0),$$

and

$$n_-(t=0) = \frac{\sigma(z)}{e(\mu_+(z) + \mu_-(z))}.$$

Simulations were conducted in the framework of the cylinder coordinates (r, z) with z directed along the vertical (altitude) and $r \perp z$. The computational area was limited to $r_{max} = 30$ km and $z_{max} \equiv H_{max} = 74$ km. At the boundary of the area, the condition $\partial F / \partial \mathbf{n} = 0$ was imposed, where $F = \{n_{run}^n, n_s, n_b, n_-, n_+\}$ and \mathbf{n} is a normal to the boundary.

The strength of a selfconsistent electric field \mathbf{E} including the external (cloud) field and the field of generated free charges was calculated by solving the current continuity equation [40, 45, 46]

$$\frac{\partial \mathbf{E}}{\partial t} = \frac{\partial \mathbf{E}_{int}}{\partial t} + \frac{\partial \mathbf{E}_{ext}}{\partial t} = -\frac{\mathbf{j}}{\varepsilon_0} + \frac{\partial \mathbf{E}_{ext}}{\partial t}, \quad (8)$$

where $\varepsilon_0 = 8.85$ pF/m, $\mathbf{E}_{int}(z, r, t)$ and $\mathbf{E}_{ext}(z, r, t)$ are the respective strengths of the charge fields and the cloud; the density of the conductivity current is

$$\mathbf{j} = en_+ \mathbf{v}_+ - en_- \mathbf{v}_- - en_s \mathbf{v}_s - en_b \mathbf{v}_b - \sum_{n=1}^N n_{run}^{(n)} \mathbf{w}_{run}^{(n)}.$$

A set responsible for optical emissions is distinguished for a detailed description of the excitation of the air species with allowance for the vibrational kinetics that permits obtaining accurate photon distributions in lines [52].

The globally most common thunderclouds have positive upper and negative bottom charges [3, 47]. Initially, the ion plasma between the cloud top and

the ionosphere shields the field above the cloud [31]. As the lightning annihilates cloud charges (intracloud discharge) or carries away the upper positive charge (cloud-to-ground lightning from the cloud with tilted dipole [31, 47]), a field of negative polarizing charges appears near the top [31]. The external field is therefore modeled by that of uniformly and negatively charged thin disk with radius R_{disk} located at the altitude H and reflected relative to the Earth’s surface ($z = 0$ km) and the lower electrosphere boundary ($z = 60$ km).

Two models of switching on the field were simulated.

The first model assumes a variable disk radius R_{disk} calculated as

$$R_{disk}(t) = \begin{cases} \sqrt{q(t)/2\pi\varepsilon_0 E_{max}}, & t \leq t_{disch}, \\ \sqrt{Q_{max}/2\pi\varepsilon_0 E_{max}}, & t \geq t_{disch}, \end{cases} \quad (9)$$

such that the charge density is

$$\sigma_{disk} = q(t)/\pi R_{disk}^2(t) = \text{const} = 2\varepsilon_0 E_{max}.$$

Here, $q(t) = Q_{max}(t/t_{disch})$ is the instantaneous charge value, Q_{max} is the maximum charge value, t_{disch} is the duration of the lightning discharge switching on the field, and E_{max} corresponds to the overvoltage

$$\delta_{max} = \frac{eE_{max}}{F_{min}P(z)} = 7$$

accepted at the disk surface. The other model assumes $R_{disk} = \text{const}$, such that the charge density is varied according to the formula $\sigma(t) = q(t)/\pi R_{disk}^2$.

Results for the 10-group RE concentration $n_{run}(r, z, t, \varepsilon_i)$ and $t_{disch} = 1$ ms are discussed below only for three pairs of Q_{max} and H (100 C, 10 km; 130 C, 14 km; and 200 C, 14 km).

3. RESULTS OF SIMULATION OF HIGH-ALTITUDE OPTICAL PHENOMENA

Space–time evolution of charged particle concentrations, field strengths, and air fluorescence were the result of simulations. The fluorescence into four main air bands was computed: the first positive system 1P ($\lambda = 570\text{--}1040$ nm, transitions $B^3\Pi_g \rightarrow A^3\Sigma_u^+$ of N_2), the Meinel system M ($\lambda = 500\text{--}2000$ nm, transitions $A^2\Pi \rightarrow X^2\Sigma$ of N_2^+), the second positive 2P, and the first negative system 1N ($\lambda = 290\text{--}530$ nm, transitions $C^3\Pi_u \rightarrow B^3\Pi_g$ of N_2 and $B^2\Sigma_u \rightarrow X^2\Sigma_g^+$ of N_2^+).

Qualitatively, the results for optical phenomena are close to those given by the previous 1.5D model [45, 46], but the glow brightness is larger. We note that neither

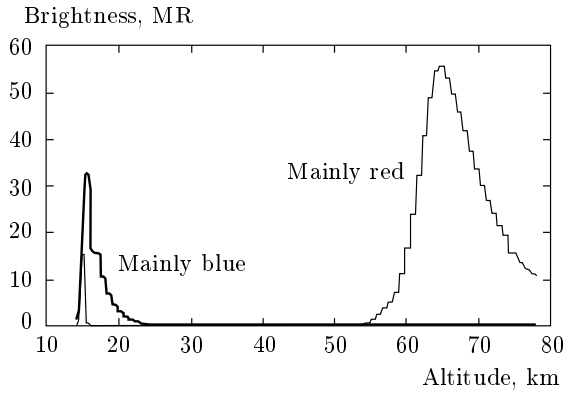


Fig. 1. Altitude fluorescence distribution; $Q_{max} = 130$ C, $H = 14$ km, and variable R_{disk}

TGFs nor TNFs were simulated in [45, 46]. The calculated brightness and color of the fluorescence, and its space–time evolution in general agree with the observational data on Blue Jets and Red Sprites [32, 34, 35]. In Fig. 1, for the sake of illustration, we present the altitude distribution of the fluorescence brightness along the discharge axis only for $Q_{max} = 130$ C, $H = 14$ km and the variable disk radius R_{disk} . Mainly high-energy REs and relaxing secondary electrons excite the lower glow (14–24 km). The upper glow above 54 km is excited by the background and secondary electrons that are in equilibrium to the local field. Background electrons account for the upper maximum, while the secondary electrons excite only in the range 55–63 km. The blue system 2P contribute to the lower glow and the red systems 1P and 1N contribute to the upper one. It is therefore natural to assume that the lower and upper glows respectively account for the Blue Jets and Red Sprites.

The fluorescence duration caused by RREAs is ~ 1 ms. In agreement with an indication in [57], the very long duration of the glow in the vicinity of the disk (Blue Jet), ~ 100 ms, was found from our calculations to be a consequence of the fluorescence owing to the prolonged recombination of positive and negative ions after ceasing of RREAs generation.

The general agreement of the calculated characteristics of the optical emissions with the observational data of high-altitude optical phenomena testifies both to the UAD model adequacy and to the trustworthiness of the computed dependences of the RE concentration on spatial coordinates and time, required for calculating TGF and TNF characteristics.

For all the configurations discussed (Q_{max} , $H = 100$ C, 10 km; 130 C, 14 km; 200 C, 14 km) and

either version of switching on the field, the RE flux is mainly concentrated in the domain adjacent to the disk (thundercloud), i.e., in the Blue Jet domain.

Proceeding from the TGF characteristic time being close to the duration of Red Sprites and much shorter than that of Blue Jets, Nemiroff et al. [50] connected the TGFs with Red Sprites. However, the duration of the pulse of REs capable of emitting hard bremsstrahlung and concentrated mainly within the Blue Jet domain is ~ 1 ms, whereas the prolonged Blue Jet fluorescence, ~ 100 ms, as pointed out above, is the radiation of decaying plasma.

4. TERRESTRIAL GAMMA-RAY FLASHES

To interpret the TGFs, the number of bremsstrahlung photons emitted by UAD into a solid angle

$$\Delta\Omega = S_{det}(\xi/H_{orbit})^2$$

in the direction to the satellites BETSI [7] and RHESSI [8] and capable of achieving the orbit altitude H_{orbit} was calculated by integrating over the domain populated by REs:

$$N_{\gamma}^{(i)} = \frac{dN_{\gamma}}{dt} f_2(\bar{\epsilon}_i, \bar{\mu}) \Delta\Omega \Delta_i \times \int_H^{H_{max}} dz P(z) g(z) \exp\left(-\frac{l_{opt}(z)}{\lambda_i}\right), \quad (10)$$

where dN_{γ}/dt is the rate of the bremsstrahlung generation per one RE ($\approx 1.045 \cdot 10^7$ s $^{-1}$ ·atm $^{-1}$ almost independent of δ [58]); $f_2(\bar{\epsilon}_i, \bar{\mu})$ is the steady-energy and angular photon distribution function [58]; $\bar{\mu}$ is the mean cosine of the angle between the photon propagation direction and the local electric force $-e\mathbf{E}$; S_{det} is the detector efficient area; i is the number of energy channel of the detector of radiation with the mean energy $\bar{\epsilon}_i$, Δ_i is a share of photons emitted into the channel i ;

$$l_{opt}(z) = \frac{h_{char}}{\xi} \exp\left(-\frac{z}{h_{char}}\right)$$

is the optical length of the air layer between the altitudes z , where UAD develops, and the orbit altitude ($H_{orbit} \gg z$); $h_{char} = 7.1$ km is a characteristic length of the “exponential” atmosphere; ξ is the cosine of the angle between the direction from the γ -source to the satellite and the vertical; and $\lambda_i = \lambda(\bar{\epsilon}_i)$ is the range of photons with the energy $\bar{\epsilon}_i$ at $P = 1$ atm [59].

In view of the uncertainty of the satellite location relative to the TGF sources and RE flux direction relative to the vertical, calculations were carried

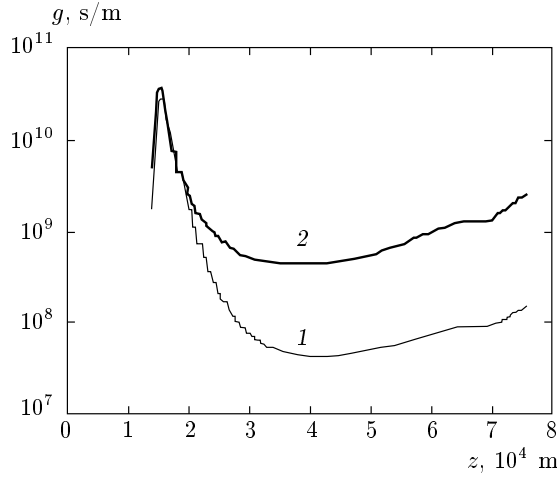


Fig. 2. The function $g(z)$ defined in (11) for two values of the cloud charge $Q_{max} = 130$ C (1), 200 C (2) at the altitude $H = 14$ km

out for several values of $\bar{\mu}$ and ξ , taking into account that a decrease in ξ increases the absorption because $l_{opt}(z)$ grows and $f_2(\bar{\varepsilon}_i, \bar{\mu})$ sharply decreases as $\bar{\mu}$ decreases [58].

The function $g(z)$ involved in formula (10) is given by the time-integrated 10-group linear concentration of REs:

$$g(z) = \sum_{i=1}^{10} \int_0^{t_{max}} dt \int_0^{r_{max}} n_{run}^{(i)}(r, z, t) \cdot 2\pi r dr, \quad (11)$$

where $n_{run}^{(i)}(r, z, t)$ is the instantaneous local concentration of REs in group i and $t_{max} = 3$ ms is the time at which the RE pulse terminates. The function is presented in Fig. 2 for $Q_{max} = 130$ C and $Q_{max} = 200$ C located at the altitude $H = 14$ km.

Below 20 km, $g(z)$ is practically identical for both Q_{max} values. At large altitudes, in the case where $Q_{max} = 200$ C, $g(z)$ is generally larger than for $Q_{max} = 130$ C, but the integrals

$$G = \int_H^{H_{max}} g(z) dz$$

differ only by a factor of 1.8: $G = 1.35 \cdot 10^{14}$ s for 200 C and $G = 7.62 \cdot 10^{13}$ s for 130 C.

The difference at large altitudes is related to different cloud charges Q_{max} and their spatial size. In the case of larger Q_{max} , the field at high altitudes is stronger, and therefore REs penetrate to higher altitudes. The proximity to G is related to REs being concentrated at lower altitudes and with a nonlinear self-

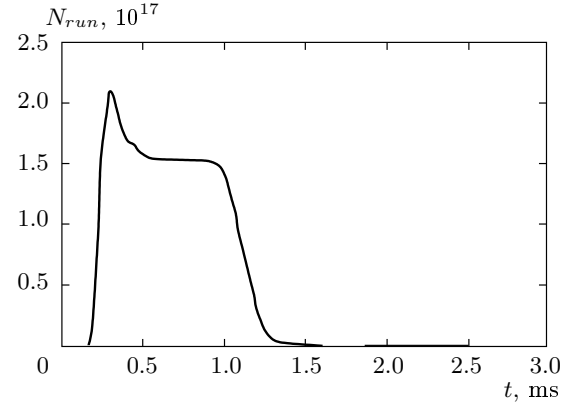


Fig. 3. Time dependence of the total RE number $N_{run}(t)$. Cloud charge $Q_{max} = 200$ C at the altitude $H = 14$ km

consistent mode of the discharge development. Generation of a large amount of low-energy charge carriers by RREAs leads to the field relaxation and RREA termination. At larger Q_{max} , the RREAs develop faster in a particular spatial domain, but also damp faster.

The emission of photons with energies from 20 keV to 20 MeV was calculated. Some results are presented in Tables 1–3 and Figs. 3–5, to be compared with observations aboard BATSE [7] and RHESSI [8].

Nemiroff et al. [50] presented processed BATSE data obtained in four energy channels: 20–50 keV, 50–100 keV, 100–300 keV, and 300–1000 keV. In our calculations, the boundaries of the first four energy ranges fit the BATSE channels. The boundaries of the remaining ranges were selected arbitrarily, but such that a sufficient number of points guarantee proximity to the continuous photon energy distribution. The duration of individual registered TGF is ~ 0.5 –5 ms. The computed γ -flash duration is specified by the RE pulse

$$N(t)_{run} = \sum_{i=1}^{10} \int_H^{H_{max}} dz \int_0^{r_{max}} n_{run}^{(i)}(r, z, t) \cdot 2\pi r dr, \quad (12)$$

and its duration is ~ 1 ms. The RE pulse for one configuration is demonstrated in Fig. 3.

The total number of photons per TGF in the range of four channels of the BATSE detector in the range 20–1000 keV was estimated in [50] by the value $N_\gamma \sim 100$ –700, which is consistent with $(N_\gamma \approx 153)$ $\bar{\mu} = \xi = 0.5$ and $(N_\gamma \approx 1105)$ $\bar{\mu} = \xi = 0.7$ calculated for $Q_{max} = 130$ C and $(N_\gamma \approx 1499)$ $\bar{\mu} = \xi = 0.5$ for $Q_{max} = 200$ C. The photon energy $\bar{\varepsilon}_\gamma = 1.26$ MeV calculated for $Q_{max} = 200$ C and $\bar{\mu} = \xi = 0.5$ corresponds to the photon energy ~ 1 MeV in TGFs [7].

Table 1. γ -emission in energy channels i with boundaries ε_1 and ε_2 , $Q_{max} = 130$ C, $H = 14$ km, $H_{orbit} = 500$ km, and $S_{det} = 0.2$ m² [7]

| i | ε_1 , keV | ε_2 , keV | $\bar{\varepsilon}_i$, keV | $N_\gamma^{(i)}$ | | |
|--|-----------------------|-----------------------|-----------------------------|-----------------------|-------------------------|-------------------------|
| | | | | $\bar{\mu} = \xi = 1$ | $\bar{\mu} = \xi = 0.7$ | $\bar{\mu} = \xi = 0.5$ |
| 1 | 20 | 50 | 35 | $4.1 \cdot 10^3$ | 90.04 | 8.2 |
| 2 | 50 | 100 | 75 | $4.1 \cdot 10^3$ | 34.03 | 6.4 |
| 3 | 100 | 300 | 200 | $10.5 \cdot 10^3$ | 146.6 | 11.6 |
| 4 | 300 | 1000 | 650 | $41.6 \cdot 10^3$ | 231.01 | 12.1 |
| 5 | 1000 | 3000 | 2000 | $2.41 \cdot 10^5$ | 679.9 | 19.4 |
| 6 | 3000 | 5000 | 4000 | $2.84 \cdot 10^5$ | 435.2 | 10.4 |
| 7 | 5000 | 7000 | 6000 | $3.4 \cdot 10^5$ | 317.05 | 34.2 |
| 8 | 7000 | 9000 | 8000 | $3.23 \cdot 10^5$ | 186.6 | 20.7 |
| 9 | 9000 | 11000 | 10000 | $3.28 \cdot 10^5$ | 257.5 | 15.7 |
| 10 | 11000 | 15000 | 13000 | $4.25 \cdot 10^5$ | 85.8 | 2.69 |
| 11 | 15000 | 20000 | 17500 | $2.66 \cdot 10^5$ | 23.7 | 0.68 |
| Number of photons $\sum_{i=1}^4 N_\gamma^{(i)}$ | | | | $6.03 \cdot 10^4$ | 553 | 38 |
| Calculated photon mean energy at the detector $\bar{\varepsilon}_\gamma$, MeV | | | | 8.7 | 3.94 | 3.0 |

In Fig. 4, the calculated relative photon distributions in four channels

$$\Delta_i = N_\gamma^{(i)} / \sum_1^4 N_\gamma^{(i)}$$

are compared to some of the BATSE TGFs processed in [50]. The agreement is satisfactory.

In Fig. 5, the calculated photon energy spectra $dN_\gamma/d\varepsilon_\gamma$ are compared with the spectrum detected aboard RHESSI [8]. The spectra calculated with $Q_{max} = 200$ C, $\bar{\mu} = \xi = 0.5$, and $\bar{\mu} = \xi = 0.7$ match the measured spectrum best of all. The computed primary emission spectrum presented in the same figure is softer than the measured spectrum and the calculated spectra at the satellite altitudes. For $Q_{max} = 130$ C and $H = 14$ km, the spectra at the satellite altitudes are harder than for $Q_{max} = 200$ C and $H = 14$ km.

The RHESSI photon spectrum is harder than the BATSE spectrum. The mean energy of photons detected by RHESSI is in the range 1–4 MeV, with ~ 2 MeV prevailing in contrast to the BATSE 1 MeV. The mean calculated photon energies behave

correspondingly, as is illustrated in Table 3, where $\bar{\varepsilon}_\gamma = 1.27$ –4 MeV.

5. TERRESTRIAL NEUTRON FLASHES

The consistency of the calculated γ -ray characteristics with TGFs, especially for $Q_{max} = 200$ C and $H = 14$ km, also testifies to the model adequacy. Therefore, the γ -ray characteristics in the source are reliable for calculating the numbers of photonuclear neutrons from UAD.

The integral yield of photonuclear neutrons from UAD was calculated in two ways: using the approximation of chaotic photon motion

$$N_n = 2cN_L \iint n_\gamma(\mathbf{r}, t) P(z) \times \int_{\varepsilon_{th}(\gamma, n)}^{\varepsilon_{\gamma, max}} f_\gamma(\delta, \varepsilon_\gamma) \sigma(\gamma, S_n) d\varepsilon_\gamma dV dt, \quad (13)$$

Table 2. γ -emission in energy channels i with boundaries ε_1 and ε_2 , $Q_{max} = 200$ C, $H = 14$ km, $H_{orbit} = 500$ km, and $S_{det} = 0.2$ m² [7]

| i | ε_1 , keV | ε_2 , keV | $\bar{\varepsilon}_i$, keV | $N_\gamma^{(i)}$ | | |
|--|-----------------------|-----------------------|-----------------------------|-----------------------|-------------------------|-------------------------|
| | | | | $\bar{\mu} = \xi = 1$ | $\bar{\mu} = \xi = 0.7$ | $\bar{\mu} = \xi = 0.5$ |
| 1 | 20 | 50 | 35 | $3.85 \cdot 10^4$ | 911 | 88.8 |
| 2 | 50 | 100 | 75 | $3.42 \cdot 10^4$ | 808 | 68.4 |
| 3 | 100 | 300 | 200 | $7.17 \cdot 10^4$ | 1280 | 116 |
| 4 | 300 | 1000 | 650 | $1.48 \cdot 10^5$ | 1410 | 102 |
| 5 | 1000 | 3000 | 2000 | $4.25 \cdot 10^5$ | 1749.7 | 86.8 |
| 6 | 3000 | 5000 | 4000 | $4.29 \cdot 10^5$ | 764.1 | 25.8 |
| 7 | 5000 | 7000 | 6000 | $4.89 \cdot 10^5$ | 483.7 | 15.3 |
| 8 | 7000 | 9000 | 8000 | $4.59 \cdot 10^5$ | 549.04 | 8.42 |
| 9 | 9000 | 11000 | 10000 | $4.61 \cdot 10^5$ | 368.4 | 5.91 |
| 10 | 11000 | 15000 | 13000 | $5.97 \cdot 10^5$ | 122.8 | 367 |
| 11 | 15000 | 20000 | 17500 | $3.73 \cdot 10^5$ | 38.9 | 1.05 |
| Number of photons $\sum_{i=1}^4 N_\gamma^{(i)}$ | | | | $2.93 \cdot 10^5$ | 4410 | 375 |
| Calculated photon mean energy at the detector $\bar{\varepsilon}_\gamma$, MeV | | | | 7.99 | 2.17 | 1.26 |

and assuming that the neutrons are generated along the photon range $\lambda_\gamma(z) = \lambda_\gamma(0)/P(z)$:

$$N_n = 2N_L \lambda_\gamma(0) \frac{dN_\gamma}{dt} \iint n_\gamma(\mathbf{r}, t) P(z) \times \int_{\varepsilon_{th}(\gamma, n)}^{\varepsilon_{\gamma, max}} f_\gamma(\delta, \varepsilon_\gamma) \sigma(\gamma, Sn) d\varepsilon_\gamma dV dt. \quad (14)$$

Here, $n_\gamma(\mathbf{r}, t)$ is the photon concentration ($n_\gamma(\mathbf{r}, t) \approx n_{run}(\mathbf{r}, t)$ [58]); $N_L \approx 2.7 \cdot 10^{25}$ m⁻³ is the Loshmidt number; $f_\gamma(\delta, \varepsilon_\gamma)$ is the steady photon distribution over energies ε_γ normalized to unity [58]; $\sigma(\gamma, Sn)$ is the total cross section of (γ, n) -reactions [60]; $\varepsilon_{th}(\gamma, 1n)$ is the $(\gamma, 1n)$ -reaction threshold; $\varepsilon_{\gamma, max}$ is the maximum energy up to which data on the cross sections are available. Within the accuracy of the present calculations, it is sufficient to let the atmosphere to consist of the ¹⁴N nuclei, for which $\varepsilon_{th}(\gamma, 1n) = 10.55$ MeV and $\varepsilon_{\gamma, max} = 29.5$ MeV [60]. In this energy range, $\lambda_\gamma(0) \approx 500$ m [59].

The calculated neutron yield values $N_n \sim 10^{14}$ – 10^{15} presented in Table 4 are consistent with the analytic es-

timate $N_n \sim 10^{15}$ [18–20] obtained for the cloud charge $Q_{cloud} = 210$ C and $H = 18$ km with allowance for the geomagnetic field, which apparently compensated the effect of the air density lower than in the present simulations ($H = 14$ km).

6. DISCUSSION

In accordance with the energy dependence of the photon range, the primary emission at different altitudes contribute to the detector readings in different energy ranges [47, 49]. To clarify the results for TGFs presented above, contributions of photons emitted at different emission altitudes were calculated (Fig. 6). The altitudes of 30–40 km contribute to low energies (tens of keV), whereas the “detected” photons of the MeV range originate from 17–20 km.

Although the low-energy photons dominate in the primary bremsstrahlung spectrum at all altitudes, they are strongly absorbed in the atmosphere. Only those of these photons are capable of escaping into space that are emitted at high altitudes, where the atmo-

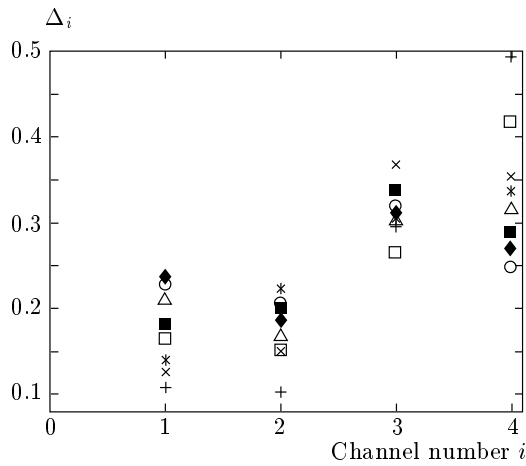


Fig. 4. Relative distribution of photons in four energy channels BATSE $\Delta_i = N_\gamma^{(i)} / \sum_1^4 N_\gamma^{(i)}$ for two values of the cloud charge Q_{max} at the altitude $H = 14$ km and two orientations of the satellite relative to the γ -source. Ref. [50]: Fig. 1b (+), Fig. 1d (\times), Fig. 1f (\blacksquare), Fig. 1l ($*$). Simulations: 130 C (\square , \triangle), $\mu = \xi = 0.7$ (\square), 0.5 (\triangle); 200 C (\circ , \blacklozenge), $\mu = \xi = 0.7$ (\circ), 0.5 (\blacklozenge)

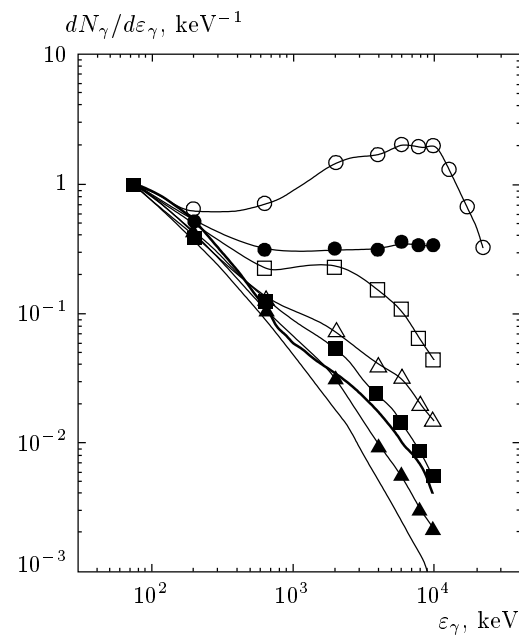


Fig. 5. Relative photon energy distribution at RHESSI for two values of the cloud charge Q_{max} at the altitude $H = 14$ km and three orientations of the satellite relative to the γ -source. The distribution at 75 keV is taken for unity. Thick line — [8], thin line — emission spectrum; 130 C (\triangle , \square , \circ); 200 C (\blacktriangle , \blacksquare , \bullet); $\mu = \xi = 0.5$ (\triangle , \blacktriangle), 0.7 (\square , \blacksquare), 1 (\circ , \bullet)

Table 3. Mean calculated photon energies for RHESSI, $H_{orbit} = 550\text{--}600$ km [8]

| | | | | |
|---------------------------------|-----|-----|------|-----|
| Q_{max}, C | 130 | | 200 | |
| $\bar{\mu} = \xi$ | 0.5 | 0.7 | 0.5 | 0.7 |
| $\bar{\varepsilon}_\gamma, MeV$ | 3 | 4 | 1.27 | 2.1 |

Table 4. (n, γ) neutron yield per discharge

| | | | | |
|-----------------------|---|-----|-----|------|
| Q_{max}, C | | 100 | 130 | 200 |
| H, km | | 10 | 14 | 14 |
| $\frac{N_n}{10^{14}}$ | Chaotic photon motion, formula (13) | 1.6 | 2.5 | 3.6 |
| | Generation along photon range, formula (14) | 4.9 | 7.6 | 10.7 |

sphere is rarefied and the absorption is weaker. But the bremsstrahlung efficiency is low in rarefied media.

The high-energy photons reaching the satellite altitudes originate mainly from the altitudes where the RE population is maximal, because such photons experi-

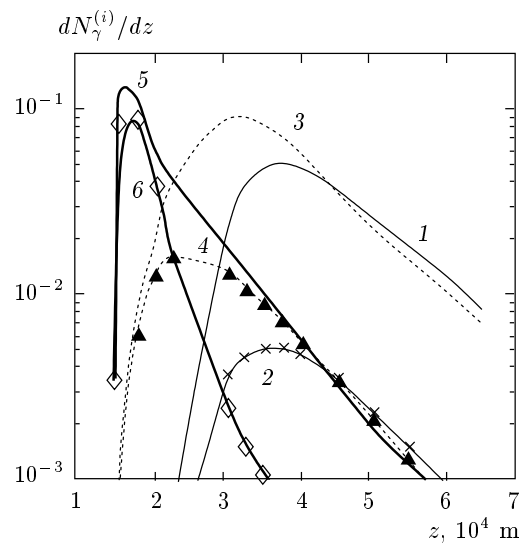


Fig. 6. The contribution of γ -emission at different altitudes $dN_\gamma^{(i)}/dz$ to the total number of photons detected by channel i for two values of the cloud charge Q_{max} at the altitude $H = 14$ km and one orientation of the detector relative to the γ -source: $\mu = \xi = 0.7$; $i = 2$ (50–100 keV), 200 C (1), 130 C (2, \times); $i = 4$ (300–1000 keV), 200 C (3), 130 C (4, \blacktriangle); $i = 6$ (3–5 MeV), 200 C (5), 130 C (6, \diamond)

ence weaker absorption. Above the RREA termination altitudes, the photon generation rate sharply reduces due to both a decrease in the RE local concentration and a strong decrease in the frequency of electron collisions with neutrals because of the exponential reduction of the atmosphere density. Thus, the absorption of low-energy photons is the reason of the detected spectra being harder than the primary emission spectrum.

The differences in the results of calculations for $Q_{max} = 130$ C and $Q_{max} = 200$ C at $H = 14$ km ensue from the corresponding RE distributions at large altitudes. The total numbers of REs N_{run} are rather close in both cases, but at high altitudes, N_{run} is ten times higher for $Q_{max} = 200$ C than for $Q_{max} = 130$ C (cf. Fig. 2). For $Q_{max} = 200$ C, there are more REs at altitudes above 20 km, and therefore the bremsstrahlung spectrum is softer.

Too large values of the photon mean energy $\bar{\varepsilon}_\gamma$ calculated at $\bar{\mu} = \xi = 1$ (Tables 1 and 2) are related to the angular distributions $f_2(\bar{\varepsilon}_i, \mu)$ of photons emitted in different energy ranges specified by $\bar{\varepsilon}_i$. The high-energy photons are emitted mainly into small angles relative to the field vector, whereas the angular distribution of low-energy photons is significantly wider (cf. Fig. 5 in [58]). Because the emission spectrum is enriched by high-energy photons at $\bar{\mu} = \xi = 1$ if compared with $\bar{\mu} = \xi = 0.5$ and 0.7, the calculated spectrum at the satellite altitudes contains more such photons.

We note that the fluorescence brightness calculated here, even if averaged over the TV chamber frame duration with the instrumental sensitivity $\langle J \rangle$ taken into account [32], exceeds the observed brightness [32] by more than an order of magnitude. For the chosen configurations, the discrepancy could be eliminated by increasing the duration t_{disch} of the lightning discharge switching on the field above the cloud. The simplified 1.5D model predicted that the increase in t_{disch} up to 30 ms leads to more than an order of magnitude decrease in $\langle J \rangle$ [45, 46] stemming from early start of the field shielding by secondary plasma above the cloud. Consequently, an increase in t_{disch} would shift the upper boundary of the $\bar{\mu}$ and ξ values to unity, fitting the calculated photon numbers with observations. The shift of ξ to unity is reasonable in view of the analysis of Cummer et al., who placed lightning discharges possibly triggered by RHESSI TGFs rather close to the RHESSI subsatellite point [48]. However, extremely large required computational time makes 2D multigroup simulations with t_{disch} significantly increased above the 1 ms value assumed here absolutely unrealistic.

As in most of the previous works, including recent papers [47, 49], the model presented here discounts ef-

Table 5. RE numbers at the BETSI detector, $H_{orbit} = 500$ km, $S_{det} = 0.2$ m² [7]

| Q_{max}, C | 130 | 200 |
|----------------------------------|---------------------|---------------------|
| H, km | 14 | |
| RE numbers escaping into space | $4.7 \cdot 10^{16}$ | $7.6 \cdot 10^{17}$ |
| RE numbers entering the detector | $4 \cdot 10^4$ | $6 \cdot 10^5$ |

fects of the magnetic field of the UAD current and the geomagnetic field. Due to an extremely low current density, the effects of the former are negligible in comparison with the action of the electric field. This is not the case with the geomagnetic field [21, 22]. For instance, the reduced electric strength 400 kV/m·atm, for which Dwyer and Smith [49] simulated RHESSI TGFs, is comparable to

$$\frac{cB_{geo}}{P(z)} = cB_{geo} \exp \frac{z}{h_{char}}$$

even at the lowest simulated γ -source altitudes $z = 15$ and 30 km [49]. For the horizontal inductance of the field in the tropical zone $B_{geo} = 40\mu$ T and for $h_{char} = 7.1$ km, we actually have $cB_{geo}/P(z) \approx 100$ and 821 kV/m·atm.

A significant number of REs can escape into outer space and contribute to the instrument readings aboard the satellites. The calculated numbers N_{run} of REs that escape into space and the numbers $N_{det} \sim N_{run} S_{det} / H_{orbit}^2$ that could irradiate the BETSI detector are presented in Table 5. Because electrons interact with matter more efficiently than photons of the same energy, their possible effects on detectors should be taken into account. However, a caveat deserves mentioning: the bending of RE trajectories by the geomagnetic field [1, 61] (see also [3]) could prevent RE escaping into space [21, 22]. On the other side, at low latitudes, where the effects of the geomagnetic field are expected to be maximal, the UADs were observed to propagate to very high altitudes close to the vertical [33].

According to our simulations, the TGFs appear self-consistently with Blue Jets and Red Sprites. But the TGFs for which high-energy REs are required are not correlated with large variations in the cloud charge moment Ql_Q caused by lightning and inherent to Red Sprites [47, 48, 62]. TGFs are correlated with vertical moment changes $\Delta Ql_Q = 20\text{--}200$ C·km [47] in contrast to much larger $\Delta Ql_Q = 500$ C·km observed in most of the sprite-associated lightning discharges [48, 61] and

termed threshold for Sprites [47], although Sprites were observed with ΔQl_Q as small as 120 C·km [31].

The lack of TGFs at large ΔQl_Q seems to be very strange and inexplicable in the framework of the discharge controlled by RREAs series. Williams et al. [47] clarified this apparent inconsistency, pointing out that numerous observations allowed regarding the mesoscale stratiform systems of clouds “... as most often responsible for sprites”. Each such system involves at least two vast horizontally extended charge layers with the upper negatively charged layer located below 10 km [47]. Williams et al. proved that at these altitudes, gamma photons, even if they were being produced, would experience strong attenuation and could not escape to outer space [47]. Besides, is it possible at all for electrons to be energized up to the MeV range in view of the dense atmosphere and a rather weak electric field? In fact, the “spider” cloud-to-ground lightning, most typical for these systems, carries away the lower positive charge [47]. The remaining negative charge is distributed along a very vast horizontal layer. Therefore, in spite of an extremely large corresponding momentum change ΔQl_Q , the electric field of the negative charge right above the cloud is most likely not sufficient to compensate the drag effect of the dense atmosphere. Besides, the atmospheric ion plasma above the cloud shields this field, at least partially. Consequently, the overvoltage $\delta = eE/F_{min}P$ directly above the cloud hardly suffices for the electron runaway.

The most ordinary cumulonimbus thunderclouds have the positive upper charge located at altitudes 15 km (we recall that $H = 14$ km in our simulations). Williams et al. [47] showed that MeV gamma photons are rather weakly absorbed at these altitudes and are capable of escaping into outer space. The electron runaway is efficient in this case. Indeed, after positive cloud-to-ground lightning (the case of a cloud with a tilted dipole) or intracloud lightning (the case of a cloud with a vertical dipole), the field of the negative polarization charge appears above the cloud as assumed in our model. Because this charge is concentrated in a rather limited volume (if compared with mesoscale stratiform systems), exactly at the altitudes of 14–20 km, it ensures sufficient overvoltage for multiplication of high-energy electrons (cf. Fig. 2) and their runaway to MeV energies with subsequent production of hard gamma-rays.

Based on published results of observations, Williams et al. [47] rejected negative cloud-to-ground lightning flashes from clouds with a vertical dipole and positive cloud-to-ground flashes from clouds with a tilted dipole as possible sources of TGFs. They con-

centrated on intracloud flashes, which are most typical in tropics, where TGFs were detected, and stated that “... gamma rays originate in the vicinity of negative lightning leaders ...”, bridging the cloud charges and ascending above the cloud tops. They disregarded the accumulation of the negative polarization charge above a thundercloud. Besides, the limited space domain occupied by a strong electric field in front of the leader imposes a serious limitation upon the acceleration of a significant number of electrons to high energies. Overcoming this difficulty seems to be possible in the framework of electron self-acceleration in front of a polarizing channel, according to which electrons move selfconsistently with the channel propagation [3]. However, the idea of the electron acceleration in front of the leaders is inconsistent with switching off the X-ray enhancement inside thunderclouds by lightning strokes observed in [5].

In any case, it is thus established that TGFs originate from rather ordinary thunderclouds and lightning flashes with moderate or even small ΔQl_Q . Is it possible that these gamma-producing flashes are not accompanied by high-altitude air fluorescence, at least weaker than above the mesoscale systems? This is not the case in view of the observations of Giant Jets from tops of ordinary clouds [33]. We also recall that Sprites were observed with $\Delta Ql_Q \approx 120$ C·km [31]. Moreover, it is obvious that in many cases, the cumulonimbus clouds shielded the glow because of their large vertical size.

As mentioned in the Introduction, a mechanism of the Red Sprite excitation (altitudes $H_{spr} = 70$ –80 km) due to the conventional breakdown driven by low-energy electrons is being discussed [31, 47]. At large distances ($H_{spr} \gg l_Q$), the reduced strength of the field of the vertical dipole with $Ql_Q = 500$ C·km, located in the troposphere (thundercloud), with allowing for the image in the ground even along the dipole axis

$$\frac{E}{P(z)} = 2 \frac{2Ql_Q}{4\pi\varepsilon_0 H_{spr}^3} \exp \frac{H_{spr}}{h_{char}}$$

is of 1.3–3.6 kV/m·Torr. The minimal (asymptotic) value $(E/P)_{br} = 4$ kV/m·Torr required for the conventional breakdown in air at large Pd [3, 63–65] is beyond this range of E/P , although rather close to the upper boundary. The decreasing dependence of $(E/P)_{br}$ on Pd reaches the asymptotic value at $Pd \approx 10$ Torr·m [3, 63]. The corresponding values of the “interelectrode spacing” d at the altitudes ~ 70 –80 km are quite realistic: $d \approx 260$ –1050 m. These estimates disagree with $E > E_{br}$ predicted for the Sprite altitudes [31]. Note that according to our simulations the intensive upper

glow (cf. Fig. 1), responsible for the Red Sprite, is excited by background electrons without breakdown.

In contrast to [49], where photon transport from a localized source at the upper RREA end was simulated using Monte Carlo technique, formulas (10) and (11) take the γ -photon emission throughout the region populated by REs into account. However, similarly to [47], the simplified exponential photon attenuation is an obvious shortcoming of (10). Besides, formulas (10), (13), and (14) involve steady photon distributions, which are universal in the sense that they are almost independent of the overvoltage δ [58] as a consequence of the parent RE distribution being steady and universal [36]. But the RE and photon distributions in natural process are not necessarily steady and δ -independent. Currently, Monte Carlo simulations are being carried out with the computed group energy distributions of the RE concentration $n_{run}(\mathbf{r}, t, \varepsilon_i)$ directly used to calculate the γ -ray source with a subsequent simulation of γ -ray transport to the satellite altitude. The same ELIZA Monte Carlo code is being used by means of which the steady RE and photon distributions were computed [36, 58]. The code accounts for all known interactions of electrons, photons, and positrons with matter described by the modern complete libraries of elementary cross sections. These Monte Carlo calculations will eliminate the shortcoming inherent to the simplest exponential attenuation of the photon flux adopted in formula (10). Such improvements are quite necessary because accurate simulations of γ -ray transport to the satellite altitude were implemented in [49] in the framework of extremely simplified models of RREA and γ -ray source for E/P invariant in space and time.

7. CONCLUSIONS

For three configurations of thundercloud charges within the framework of the mechanism of breakdown controlled by RREA generations, 2D numerical simulations of UAD and secondary air fluorescence are presented. Their results in general agree with observations of high-altitude optical phenomena above thunderclouds.

From the calculated RE space–time distributions, bremsstrahlung characteristics were computed, from which, for a simplified exponential attenuation in the exponential atmosphere, the photon numbers and spectra were calculated at the altitudes of the satellites BETSI [7, 50] and RHESSI [8]. The computed photon numbers, photon distributions, and mean energies depend both on the configuration specified by the cloud

charge and its altitude and on the angle between the direction from the γ -source to the detector and the vertical. For sufficiently large angles, the results agree with the numbers of TGF photons and their spectra detected aboard BETSI and RHESSI. Calculations for the chosen configurations prove that TGFs originate from the altitudes 14–20 km, characteristic of the Blue Jets, where avalanche multiplication of REs occurs and the RE flux is almost entirely concentrated (cf. Fig. 2 for the function $g(z)$). This confirms conclusions of Dwyer and Smith [49] and Williams et al. [47], who proceeded from simplified models, placed the TGF origin in the upper troposphere/lower stratosphere (16–22 km).

As the general agreement of calculations with observations of Blue Jets and Red Sprites [32], the satisfactory agreement of TGF characteristics computed for small $\bar{\mu}$ and ξ with observations [7, 8, 50] testifies to the trustworthiness of the discussed model.

The numbers of neutrons generated by photonuclear reactions associated with the UAD development were calculated. For the simulated configurations, the numbers appeared to be rather large, $\sim 10^{14}$ – 10^{15} , and matched the analytic estimates in [18–20], where it was shown, however, that these numbers are too small to account for the TNFs detected in correlation with thunderstorm discharges at the Earth's surface [13–15], even at high-mountain station [13].

In this paper, TGFs and TNFs were simulated under the assumption that they originate from UADs developing in the RREA mode [9–12]. Another mechanism is conceivable based on analyses of the temporal correlation of TGFs with VLF/ELF (very low frequency/extremely low frequency) signals (50 Hz–30 kHz and < 0.1 Hz–400 Hz) [48, 62] and on a strong dependence of the γ -ray flux and spectra at satellite altitudes on the γ -source altitude [47]. The mechanism assumes electron runaway in front of upward negative leaders of intracloud lightning discharges bridging the upper positive and lower negative charges of the most typical thunderclouds with vertical dipole moments $Ql_Q = 20$ – 200 C·km [47], which are much less than the most sprite-associated moment change $\Delta Ql_Q = 500$ C·km. Electron runaway at the leader front is regarded as a possible origin of TNFs alternative to the UAD origin [20]. The capability to account for the ground-based observations [13–15] is its advantage. This origin of TGFs and TNFs is to be thoroughly studied and simulated numerically before it can be accepted or rejected.

Further research of TNFs is required. Proving that TNFs are related with atmospheric discharges would be a serious argument in favor of the breakdown mecha-

nism in the atmosphere controlled by REs [9–12]. The predicted neutron yields per TNF, $\sim 10^{14}$ – 10^{15} (UAD, Table 4) and $4 \cdot 10^{13}$ (lightning [20]) are large enough to be measured aboard an aircraft or spacecraft.

Although the results obtained here for small $\bar{\mu} = \xi$ agree with the BETSI and RHESSI TGFs, further experiments and numerical simulations are required to select a discharge type causal to TGFs and TNFs, i.e., whether UADs or the most common intracloud lightning flashes globally [47], and to develop an adequate mechanism. The TGF-correlated moment changes $\Delta Ql_Q = 11$ – 107 C·km reported in [48] and [62] are very puzzling in view of the absence of TGF in the case of much larger sprite-associated changes $\Delta Ql_Q = 500$ C·km. Up to 3 ms TGF advance relative to the lightning VLF/ELF signals is another unexpected observation [48]. The problem of the TGF advance can possibly be resolved if switching off the X-ray enhancement inside thunderclouds coincident with the lightning discharge onset is taken into account [5]. Obviously, this observation, contradicting the idea of the TGF source at the leader front [47], permits interpreting both prior- and post-lightning TGFs in a unified manner: the prior-TGFs possibly occur due to RREA series initiated by cosmic rays throughout the inner volume of the charged cloud, whereas the post-lightning TGFs are produced by RREAs above the cloud after the same lightning switches on the field above the cloud shielded by the ion plasma [31].

The authors express their deepest gratitude to R. I. Il'kaev and S. J. Gitomer for the support of research in atmospheric electricity, to A. V. Gurevich, R. A. Roussel-Dupré, E. M. Symbalisty, and K. P. Zybin for the long-term cooperation in this area.

REFERENCES

1. C. T. R. Wilson, Proc. Cambridge Phil. Soc. **22**, 534 (1924).
2. A. S. Eddington, Nature **2948** (suppl.), 25 (1926).
3. L. P. Babich, *High-energy Phenomena in Electric Discharges in Dense Gases: Theory, Experiment and Natural Phenomena*, Futurepast Inc., Arlington, Virginia, USA (2003).
4. G. E. Parks, B. H. Mauk, R. Spiger, and J. Chin, Geophys. Res. Lett. **8**, 1176 (1981).
5. M. McCarthy and G. E. Parks, Geophys. Res. Lett. **12**, 393 (1985).
6. K. B. Eack, W. B. Beasley, W. D. Rust, T. C. Marshall, and M. Stolzenburg, Geophys. Res. Lett. **23**, 2915 (1996).
7. G. J. Fishman, P. N. Bhat, R. Mallozzi, J. M. Horack, T. Koshut, C. Kouveliotou, G. N. Pendleton, C. A. Meegan, R. B. Wilson, W. S. Paciesas, S. J. Goodman, and H. J. Christian, Science **264**, 1313 (1994).
8. D. M. Smith, L. I. Lopez, R. P. Lin, and C. P. Barrington-Leigh, Science **307**, 1085 (2005).
9. A. V. Gurevich, G. M. Milikh, and R. A. Roussel-Dupré, Phys. Lett. A **165**, 463 (1992).
10. R. A. Roussel-Dupré and A. V. Gurevich, J. Geophys. Res. **101**, 2297 (1996).
11. A. V. Gurevich and K. P. Zybin, Uspekhi Fiz. Nauk **171**, 1177 (2001).
12. A. V. Gurevich and K. P. Zybin, Phys. Today **58**, 37 (2005).
13. G. N. Shah, H. Razdan, G. L. Bhat, and G. M. Ali, Nature **313**, 773 (1985).
14. A. N. Shyam and T. C. Kaushik, J. Geophys. Res. **104**, 6867 (1999).
15. B. M. Kujevskii, Bull. Moscow Univ., Ser. 3, Physics. Astronomy, № 5, p. 14 (2004).
16. R. L. Fleisher, J. A. Plumer, and K. Crouch, J. Geophys. Res. **79**, 5013 (1974).
17. R. L. Fleisher, J. Geophys. Res. **80**, 5005 (1975).
18. L. P. Babich, Pis'ma v Zh. Eksp. Teor. Fiz. **84**, 345 (2006).
19. L. P. Babich, Geomagnetizm i Aeronomiya **47**, 702 (2007).
20. L. P. Babich and R. A. Roussel-Dupré, J. Geophys. Res. **112**, D13303, doi:10.1029/2006JD008340 (2007).
21. L. P. Babich, R. I. Il'kaev, A. Y. Kudryavtsev, I. M. Kutsyk, and R. A. Roussel-Dupré, Dokl. Akad. Nauk, Earth Sci. **381**, 994 (2001).
22. L. P. Babich, R. I. Il'kaev, I. M. Kutsyk, A. Y. Kudryavtsev, R. A. Roussel-Dupré, and E. M. D. Symbalisty, Geomagnetizm i Aeronomiya **44**, 243 (2004).
23. C. T. R. Wilson, Proc. Phys. Soc. London **37**, 32D (1925).
24. V. P. Pasko, U. S. Inan, Y. N. Taranenko, and T. F. Bell, Geophys. Res. Lett. **22**, 365 (1995).
25. V. P. Pasko, U. S. Inan, and T. F. Bell, Geophys. Res. Lett. **23**, 301 (1996).

26. V. P. Pasko, U. S. Inan, T. F. Bell, and Y. N. Taranenko, *J. Geophys. Res.* **102**, 4529 (1997).
27. Yu. P. Raizer, G. M. Milikh, M. N. Shneider, and S. V. Novakovski, *J. Phys. D: Appl. Phys.* **31**, 3255 (1998).
28. G. M. Milikh and J. A. Valdivia, *Geophys. Res. Lett.* **26**, 525 (1999).
29. N. Liu and V. P. Pasko, *J. Geophys. Res.* **109**, A04301 (2004).
30. G. D. Moss, V. P. Pasko, N. Liu, and G. Veronis, *J. Geophys. Res.* **111**, A02307, doi:10.1029/2005JA011350 (2006).
31. V. P. Pasko, *Theoretical Modeling of Sprites and Jets, in Sprites, Elves and Intense Lightning Discharges*, ed. by M. Füllekrug et al., Springer, Netherlands (2006), p. 253–311.
32. D. D. Sentman and E. M. Wescott, *Phys. Plasmas* **2**, 2514 (1995).
33. V. P. Pasko, M. Stenley, J. D. Mathews, U. S. Inan, and T. G. Wood, *Nature* **416**, 152 (2002).
34. *Sprites, Elves and Intense Lightning Discharges*, ed. by M. Füllekrug et al., Springer, Netherlands (2006).
35. U. S. Inan, *C. R. Acad. Sci. Phys.* **3**, 1411 (2002).
36. L. P. Babich, E. N. Donskoy, R. I. Il'kaev, I. M. Kutsyk, and R. A. Roussel-Dupré, *Plasma Phys. Rep.* **30**, 616 (2004).
37. N. G. Lehtinen, M. Walt, U. S. Inan, T. F. Bell, and V. P. Pasko, *Geophys. Res. Lett.* **23**, 2645 (1996).
38. Yu. N. Taranenko and R. A. Roussel-Dupré, *Geophys. Res. Lett.* **23**, 571 (1996).
39. N. G. Lehtinen, V. P. Pasko, and U. S. Inan, *Geophys. Res. Lett.* **24**, 2639 (1997).
40. V. Yukhimuk, R. A. Roussel-Dupré, E. M. D. Symbalisty, and Y. Taranenko, *Geophys. Res. Lett.* **25**, 3289 (1998).
41. I. M. Kutsyk and L. P. Babich, *Phys. Lett. A* **253**, 75 (1999).
42. N. G. Lehtinen, T. F. Bell, and U. S. Inan, *J. Geophys. Res.* **104**, 24699 (1999).
43. N. G. Lehtinen, U. S. Inan, and T. F. Bell, *J. Geophys. Res.* **106**, 28841 (2001).
44. R. A. Roussel-Dupré, E. Symbalisty, Y. Taranenko, and V. Yukhimuk, *J. Atmosph. Solar-Terrest. Phys.* **60**, 917 (1998).
45. L. P. Babich, R. I. Il'kaev, I. M. Kutsyk, K. I. Bakhov, and R. A. Roussel-Dupré, *Dokl. Akad. Nauk, Earth Sci.* **388**, 106 (2003).
46. L. P. Babich, R. I. Il'kaev, I. M. Kutsyk, K. I. Bakhov, and R. A. Roussel-Dupré, *Geomagnetizm i Aeronomiya* **44**, 231 (2004).
47. E. Williams, R. Boldi, J. Bor, G. Satori, C. Price, E. Greenberg, Y. Takahashi, K. Yamamoto, Y. Matsudo, Y. Hobara, M. Hayakawa, T. Chronis, E. Anagnostou, and D. M. Smith, and L. Lopez, *J. Geophys. Res.* **111**, D16209, doi:10.1029/2006JD006447 (2006).
48. S. A. Cummer, Y. Zhai, W. Hu, D. M. Smith, L. I. Lopez, and M. A. Stanley, *Geophys. Res. Lett.* **32**, L08811, doi:10.1029/2005GL022778 (2005).
49. J. R. Dwyer and D. M. Smith, *Geophys. Res. Lett.* **32**, L22804, doi: 1029/2005GL023848 (2005).
50. R. J. Nemiroff, J. T. Bonnell, and J. P. Norris, *J. Geophys. Res.* **102**, 9659 (1997).
51. G. I. Marchuk, *Methods of Calculation of Nuclear Reactors*, Gosatomizdat, Moscow (1961).
52. A. Y. Kudryavtsev, Ph. D. Thesis, Lomonosov State Univ., Moscow (2005).
53. L. P. Babich, *High Temp.* **33**, 190 (1995).
54. L. P. Babich and M. L. Kudryavtseva, *Zh. Eksp. Teor. Fiz.* **131**, 808 (2007).
55. R. R. Daniel and S. A. Stephens, *Rev. Geophys. Space Phys.* **12**, 233 (1974).
56. Yu. N. Taranenko, U. S. Inan, and T. F. Bell, *Geophys. Res. Lett.* **20**, 2675 (1993).
57. Yu. N. Taranenko and R. A. Roussel-Dupré, *Geophys. Res. Lett.* **23**, 571 (1996).
58. L. P. Babich, E. N. Donskoy, I. M. Kutsyk, and R. A. Roussel-Dupré, *Geomagnetizm i Aeronomiya* **44**, 697 (2004).
59. D. P. Grechukhin, *Gamma-radiation*, in book: *Physical Encyclopedia*, Vol. 1, ed. by A. M. Prokhorov, Sov. Encyclopedia, Moscow (1988).
60. S. S. Dietrich and B. L. Berman, *Atom. Data Nuclear Data Tables* **38**, 199 (1988).
61. E. G. Halliday, *Proc. Cambridge Phil. Soc.* **30**, 206 (1934).
62. W. Hu, S. A. Cummer, W. A. Lyons, and T. E. Nelson, *Geophys. Res. Lett.* **29**, 1279, doi:10.1029/2001GL014593 (2002).
63. A. I. Pavlovskii, L. P. Babich, T. V. Loiko, and L. V. Tarasova, *Dokl. Akad. Nauk, Fiz.* **30**, 303 (1985).
64. J. M. Meek and J. D. Craggs, *Electrical Breakdown of Gases*, Oxford Univ. Press, London (1953).
65. Yu. P. Raizer, *Gas Discharge Physics*, Springer, Berlin (1991).